

## Surface structure of liquid Bi and Sn: An x-ray reflectivity study

P. S. Pershan,<sup>1</sup> S. E. Stoltz,<sup>1</sup> Oleg G. Shpyrko,<sup>2</sup> Moshe Deutsch,<sup>3</sup> Venkatachalamathy S. K. Balagurusamy,<sup>1</sup> Mati Meron,<sup>4</sup> Binhu Lin,<sup>4</sup> and Reinhard Streitel<sup>1</sup>

<sup>1</sup>Department of Physics and SEAS, Harvard University, Cambridge, Massachusetts 02138, USA

<sup>2</sup>Department of Physics, University of California-San Diego, San Diego, La Jolla, California 92093, USA

<sup>3</sup>Department of Physics and Institute of Nanotechnology and Advanced Materials, Bar-Ilan University, Ramat-Gan 52900, Israel

<sup>4</sup>CARS, University of Chicago, Chicago, Illinois 60637, USA

(Received 10 November 2008; revised manuscript received 12 January 2009; published 13 March 2009)

X-ray reflectivity measurements of the liquid Bi surface are presented and analyzed together with previous liquid Sn results. Published measurements on liquid Ga, In, and K all exhibit a single strong maximum at a wave-vector transfer of the order of the reciprocal of an atomic-diameter, due to surface-induced layering. In contrast, both Sn and Bi exhibit—in addition—a weak broad peak at much smaller wave-vector transfers. This feature is an unambiguous signature of an enhanced electron density in the near-surface region. Possible ways of modeling this enhancement are presented. Once the different surface-roughening effects of thermal capillary waves are accounted for, the surface structure factors of Sn and Bi are remarkably similar. The principal difference between the two is that the depth of the layering below the surface is more than  $\sim 40\%$  larger for Bi than for Sn. This is considerably larger than the ratio of their covalent radii which is only  $\sim 10\%$ . No theoretical explanation can be offered at this time for the surface structure difference between Sn and Bi and other elemental liquid metals studied to date: Ga, In, and K.

DOI: 10.1103/PhysRevB.79.115417

PACS number(s): 68.03.-g, 68.35.Ct, 61.25.Mv

### I. INTRODUCTION

Slightly over 30 years ago, Rice and co-workers<sup>1,2</sup> predicted that the atoms at the free surface of a liquid metal should be stratified to a depth of a few atomic diameters. The physical basis of this prediction is the change across the free surface between the conducting metallic liquid phase, in which the interactions are dominated by columb/quantum effects involving the free-electron Fermi gas and the liquid of positively charged ions, and the nonconducting vapor phase dominated by van der Waals interactions. According to Rice this change suppresses the short-distance fluctuations of the surface and causes atomic layering similar to that occurring at a hard wall.<sup>3</sup> The surface-induced layering phenomena that were initially confirmed by x-ray reflectivity measurements two decades later fell into two classes. For liquid Ga,<sup>4</sup> In,<sup>5</sup> and K (Ref. 6), the atomic layering was well described by a relatively simple distorted crystal model (DCM) that will be described below.<sup>7</sup> The reflectivity for liquid Hg deviated from this simple model and required a more complex one, putting it into a class by itself. Results from a subsequent experiment on liquid Sn seemed to display yet a third class of surface structure, exhibiting a layer of enhanced density at the vapor-liquid surface.<sup>8</sup>

We have carried out x-ray reflectivity measurements on the free surface of liquid Bi. These measurements show that the layered surface is capped by a single atomic layer of a density higher than that of the bulk. Thus, it appears that both Bi and Sn exhibit a similar surface structure (requiring a relatively subtle deviation from the DCM) that is different from both that of Hg and the simple DCM of Ga, In, and K.

### II. BACKGROUND

The kinematics of x-ray scattering from liquid surfaces have been discussed in a number of recent papers.<sup>8-10</sup> X rays

of wavelength  $\lambda$  are incident on the  $x$ - $y$  plane of the liquid surface at an angle  $\alpha$  with respect to the surface plane. Scattered radiation is detected at a reflectance angle  $\beta$  with respect to an  $x$ - $y$  surface plane and azimuthal angle  $\theta$  by a scintillation detector with the resolution defined by a rectangular slit of a horizontal width  $w$  and a vertical height  $h$  placed in front of the detector at a distance  $L$  from the sample. Measurements have been performed at Sector 15-ID (ChemMat-CARS) of the Advanced Photon Source. For x rays produced by an undulator beamline at a third generation synchrotron source, the incident beam is essentially parallel, monochromatic, and physically smaller than the detector slit.

For incident angles  $\alpha$  larger than four or five times the critical angle  $\alpha_c = \sqrt{\rho_\infty r_0 \lambda^2 / \pi}$ , where  $\rho_\infty$  is the electron density of the bulk liquid and  $r_0$  is the classical radius of the electron, the differential cross-section for scattering from a liquid surface can be expressed as<sup>6,11,12</sup>

$$\frac{d\Sigma}{d^2\vec{q}_{xy}} \approx A_0 \left( \frac{q_c}{2q_z} \right)^4 |\Phi(q_z)|^2 \left( \frac{q_{xy}}{q_{\max}} \right)^\eta \left( \frac{\eta}{2\pi q_{xy}^2} \right). \quad (1)$$

In this expression, the three components of the wave-vector transfer of a ray scattered into the center of the detector are

$$q_x = (2\pi/\lambda) \cos \beta \sin \theta,$$

$$q_y = (2\pi/\lambda) [\cos \beta \cos \theta - \cos \alpha],$$

$$q_z = (2\pi/\lambda) [\sin \beta + \sin \alpha]. \quad (2)$$

The first term in Eq. (1),  $A_0(q_c/2q_z)^4$ , corresponds to the scattering from an ideally flat and sharp surface (i.e., no roughness) at which the electron density changes discontinuously from the vacuum or vapor density  $\rho \approx 0$  to  $\rho_\infty$  upon crossing the  $x$ - $y$  surface plane.  $A_0$  is the cross-sectional area

of the incident beam. The surface structure factor represented by the second term,

$$\Phi(q_z) = \rho_\infty^{-1} \int dz [d\langle\rho(z)\rangle/dz] \exp[iq_z z], \quad (3)$$

accounts for the actual variation in the  $x$ - $y$ -averaged electron density  $\langle\rho(z)\rangle$  along the surface normal  $z$ . The remaining two multiplicative terms in Eq. (1) describe the effect of thermal capillary waves on the surface scattering. The effect of the liquid surface tension  $\gamma$  is expressed by the capillary exponent

$$\eta = (k_B T / 2\pi\gamma) q_z^2, \quad (4)$$

and  $q_{\max}$  represents an upper cutoff to the capillary wave vectors that is analogous to the Debye wave vector employed in modeling thermal vibrations in solids. The specular x-ray reflectivity is obtained by integrating  $d\Sigma/d^2\vec{q}_{xy}$  over the solid angle subtended by the detector slit when  $\theta=0$ ,  $\beta=\alpha$  (specular reflection),

$$\Delta\Omega \approx (2\Delta q_x)(2\Delta q_z)/(k^2 \sin \beta) \approx (w/L)(h/L)\cos \beta. \quad (5)$$

Thus the reflectivity has the form

$$R(q_z) \approx R_F(q_z) |\Phi(q_z)|^2 \int_{A_{\text{res}}^{q_{xy}}} d^2\vec{q}_{xy} (q_{xy}/q_{\max})^\eta [\eta/(2\pi q_{xy}^2)], \quad (6)$$

where  $A_{\text{res}}^{q_{xy}}$  is the projection of the slit-determined resolution on the liquid surface and

$$R_F(q_z) \approx |(q_z - \sqrt{q_z^2 - q_c^2})/(q_z + \sqrt{q_z^2 - q_c^2})|^2 \approx (q_c/2q_z)^4 \quad (7)$$

is the Fresnel reflectivity from an ideally flat, smooth, and abrupt surface.

Since there is considerable diffuse scattering from the bulk liquid below the surface, the reflectivity data typically presented are the difference between the reflectivity measured at the specular condition ( $\alpha=\beta$  and  $\theta=0$ ) [Eq. (6)] and the average of the corresponding signals measured at  $\alpha=\beta$  and the minimum possible offset  $\theta \approx \pm (w/L)$ . In the discussion below, we make use of the expedient of simply referring to this background-subtracted reflectivity data as the measured  $R$  or  $R/R_F$ , without explicitly mentioning the background subtraction.

The atomic number density profile  $\langle\rho^A(z)\rangle$  of the DCM consists of a sum of periodically spaced Gaussians with identical integrated areas,<sup>4,7</sup>

$$\frac{\langle\rho^A(z)\rangle}{\rho_\infty^A} = \sum_{n=0}^{\infty} \frac{d}{\sigma_n \sqrt{2\pi}} \exp[-(z - nd)^2/(2\sigma_n^2)]. \quad (8)$$

Taking the Gaussian widths to increase as  $\sigma_n^2 = \sigma_0^2 + n\bar{\sigma}^2$ , this model exhibits a near-surface layering that decays with increasing  $z$  and approaches eventually the uniform (normalized) bulk density of unity. The electron density is the convolution of the number density of atoms with the atomic form factor  $F(z)$ ,

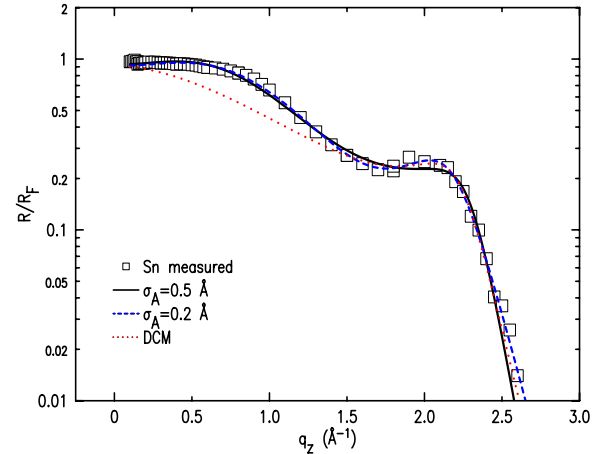


FIG. 1. (Color online) Measured Fresnel-normalized x-ray reflectivity from the surface of liquid Sn (□) previously published in Ref. 8. The solid and broken lines are the best fits of the present model discussed in the text for different  $\sigma_A$ . The dotted line is the best fit of the distorted crystal model (Refs. 7 and 8).

$$\begin{aligned} \langle\rho(z)\rangle &= \int dz' \sum_{n=0}^{\infty} \frac{d}{\sigma_n \sqrt{2\pi}} \exp[-(z - z' - nd)^2/(2\sigma_n^2)] \\ &\quad \times [F(z')/Z_{\text{eff}}], \end{aligned} \quad (9)$$

where  $Z_{\text{eff}} = Z + f'(E)$  is the energy dependent atomic scattering amplitude. The surface structure factor of the DCM has, therefore, the form

$$\begin{aligned} \Phi^{\text{DCM}}(q_z) &= i[F(q_z)/Z_{\text{eff}}] q_z d \sum_{n=0}^{\infty} \exp[iq_z dn] \exp[-\sigma_n^2 q_z^2/2] \\ &= iq_z [F(q_z)/Z_{\text{eff}}] d \frac{\exp[-\sigma_0^2 q_z^2/2]}{1 - \exp[iq_z d] \exp[-\bar{\sigma}^2 q_z^2/2]}. \end{aligned} \quad (10)$$

This  $\Phi^{\text{DCM}}(q_z)$  has the desired form observed in the measured  $R/R_F$  of Ga and In (and appears to be characteristic of K as well): it exhibits a peak at  $q_z \approx 2\pi/d$ , approaches unity as  $q_z \rightarrow 0$ , and decays to zero as  $q_z$  increases beyond the peak.

### III. REFLECTIVITY FROM TIN

The previously published  $R/R_F$  data for liquid Sn are displayed in Fig. 1. The point that was made in the original publication, and which is repeated here, is illustrated by the difference between the dotted line, which represents the best fit of the DCM to the measured layering peak at  $\sim 2.2 \text{ \AA}^{-1}$ , and the data especially in the region  $q_z < 1.4 \text{ \AA}^{-1}$ . As can be seen, the DCM (dotted line) provides a good fit in the layering peak region but greatly underestimates  $R/R_F$  at lower  $q_z$ , revealing the existence of a broad maximum centered at  $q_z = 0.7 \text{ \AA}^{-1}$  that cannot be duplicated by the basic DCM. The simplest modification to the DCM that will produce such a feature is to add one additional Gaussian, representing a layer of density  $\rho^A$ , at a position  $z_A$  above the surface,

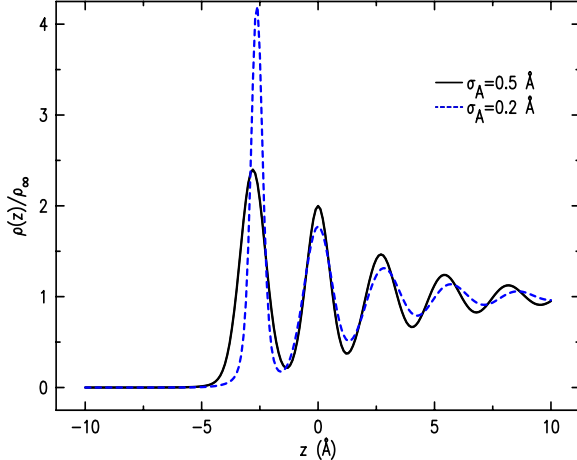


FIG. 2. (Color online) The electron densities corresponding to the two fits of the present model to the measured Sn reflectivity are shown in Fig. 1.

$$\begin{aligned} \langle \rho^A(z) \rangle &= \rho_A \frac{d}{\sigma_A \sqrt{2\pi}} \exp[-(z + z_A)^2/(2\sigma_A^2)] \\ &+ \sum_{n=0}^{\infty} \frac{d}{\sigma_n \sqrt{2\pi}} \exp[-(z - nd)^2/(2\sigma_n^2)]. \quad (11) \end{aligned}$$

This model is slightly more general than the model that was used in Ref. 8 for which  $\rho^A$  was constrained to be unity. We argue in Appendix A that the shape of this bump is a clear indication that the average electron density at the surface is higher than in the bulk. With the constraint that  $\rho^A=1$ , the only way to increase the density at the surface is to decrease the distance between this layer and the surface, i.e.,  $z_A < d$ . Thus, the high density in the near-surface region was assigned in Ref. 8 to a compression of the first layer. In fact, there are considerable cross correlations between the various fitting parameters and when one includes the possible systematic errors in the data, it is likely that the conclusion of a compression is not the only possibility. For example, the higher near-surface density can also be obtained by increasing  $\rho^A$  above unity while leaving  $z_A=d$  or even  $z_A>d$ , i.e., an expansion of the first layer. The fact that alternative fits of the modified DCM are possible is illustrated in Fig. 1 with an expanded first layer (fixed  $\sigma_A=0.5$  Å, yielding  $z_A=1.05d$  and  $\rho^A=1.27$ , solid line) and with a compression of the first layer (fixed  $\sigma_A=0.2$  Å, yielding  $z_A=0.95d$  and  $\rho^A=1.03$ , dashed line). These examples demonstrate that there seems to be no physical basis for constraining  $\rho^A$  to unity. The electron densities corresponding to the two fits in Fig. 1 are shown in the same lines in Fig. 2.

In fact, the two fits in Figs. 1 and 2 are just two examples. The data shown in Fig. 3 summarize three of the parameters [ $\rho^A$ ,  $\Delta d/d=(z_A-d)/d$ , and  $\sigma_0$ ] for one set of fits. For these fits,  $\sigma_A$  was constrained at values that vary from 0.1 to 0.6 Å. The data in Fig. 3(a) illustrate the fact that although the integral over the adlayer's density is only weakly dependent of the Gaussian width of that layer, its value only matches the value used in Ref. 8 for small values of  $\sigma_A$ . The

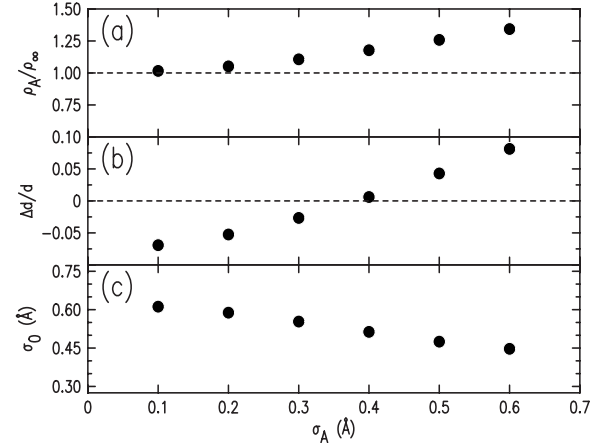


FIG. 3. Parameters derived from the best-fit models for the Sn data as a function of the different fixed values of  $\sigma_A$ .

present result that is shown in Fig. 3(b) is that the spacing between the adlayer and the first layer of the DCM changes from the compressed layer for small  $\sigma_A$  that was concluded in Ref. 8 to a dilated layer for larger values of  $\sigma_A$ , while the quality of the fit remains essentially the same. Figure 3(c) illustrates the cross correlation between the best-fit value of the width of the first layer in the DCM and  $\sigma_A$ .

One consequence of the discussion above is that it is not possible to provide a unique representation for the detailed structure of the near-surface electron density for Sn. Different models can reproduce the increased density at the surface; however, while the two best fits for  $R/R_F$  shown in Fig. 2 are only slightly different, the corresponding two electron densities in Fig. 2 are qualitatively different. Although the shapes of the oscillations below the surface vary only slightly, the difference in the amplitude of the adlayer varies by nearly a factor of 2.

#### IV. REFLECTIVITY FROM BISMUTH

The background-subtracted  $R/R_F$  data for Bi are shown in Fig. 4. Unlike the Sn data, the Bi reflectivity has not previously been measured and it is presented here. For comparison, the  $R/R_F$  for Sn is also shown. The order-of-magnitude difference in  $R/R_F$  between Sn and Bi at  $q_z \approx 2$  is caused by the lower surface tension of Bi. The dash-dotted line illustrates that the predicted reflectivity from an interface with the same surface tension as Bi but without layering ( $\Phi=1$ ) can clearly not account for the measured  $R(q_z)$ . The method by which this surface tension is determined is illustrated by the off-specular diffuse scattering (i.e.,  $\beta \neq \alpha$ ,  $\theta=0$ ) as a function of  $q_y$  for  $\alpha=4.35^\circ$  ( $q_z \approx 1$  Å<sup>-1</sup>) shown in Fig. 5. The solid line through the data is the best fit that was obtained for a surface tension of 385 mN/m, corresponding to a value of  $\eta \approx 0.32$  [Eq. (4)]. An identical analysis for Sn shown in Fig. 3 of Ref. 8 yielded a best-fit value of 560 mN/m for the surface tension of Sn.<sup>8</sup>

To understand the effect of the surface tension  $\gamma$ , note that for Sn  $\gamma=560$  mN/m at  $T=513$  K yields  $\eta=0.80$  at  $q_z \approx 2.0$  Å<sup>-1</sup>, while for Bi  $\gamma=385$  mN/m at  $T=555$  K yields

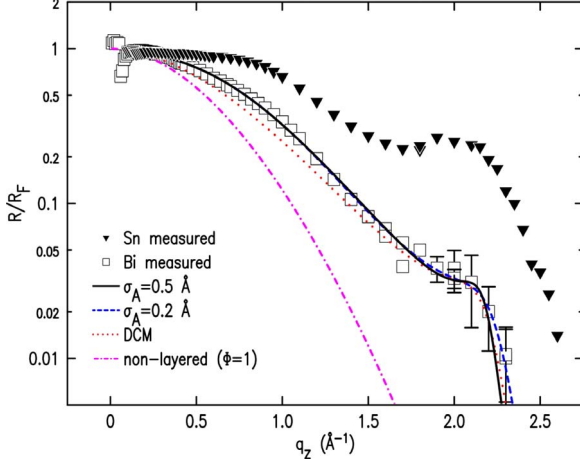


FIG. 4. (Color online) Measured Fresnel-normalized x-ray reflectivity of Bi ( $\square$ ) and Sn ( $\blacktriangledown$ ). The model fits discussed in the text are shown as lines. The two fits of the present model for different  $\sigma_A$  are distinguishable only at the largest  $q_z$ . The dotted line is the best fit of the distorted crystal model (Ref. 7). The dash-dotted-dash line shows the reflectivity that would be expected if for a simple interface with no layering ( $\Phi=1$ ) and the same surface tension as liquid Bi.

$\eta=1.3$  at the same  $q_z$ . Although the difference between  $\eta=1.3$  and 0.8 may not appear that significant, since  $\eta$  appears in the exponent of the integrand in Eq. (6), the result is approximately exponential in  $\eta$ . As shown by the increasing size of the error bars as  $q_z \geq 2.0 \text{ \AA}^{-1}$  ( $\eta \geq 1.2$ ), this has a dramatic effect on the reflectivity.<sup>12</sup>

The practical consequence of the delicate nature of reflectivity measurements at  $\sqrt{q_x^2 + q_y^2 + q_z^2} \approx q_{\text{peak}}^{\text{bulk}} \sim 2 \text{ \AA}^{-1}$ , where the diffuse scattering from the bulk liquid structure factor also peaks, is to increase the uncertainty in the best-fit value of the Bi layer spacing  $d$ . Although the best-fit values for the layer spacing  $d$  vary somewhat with  $\sigma_A$ , they always fall within 1%–2% of 2.83 Å which is slightly less than the atomic diameter of 3.1 Å.<sup>13</sup> Both of these values are also

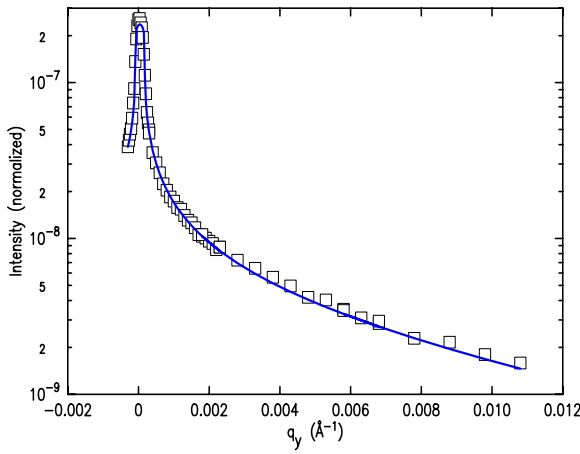


FIG. 5. (Color online) Measured scattered intensity ( $\square$ ) from the liquid Bi surface along the  $q_y$  axis at a fixed  $q_z \approx 1.0 \text{ \AA}^{-1}$ . The solid line is the best fit of Eq. (1), yielding a surface tension of 385 mN/m.

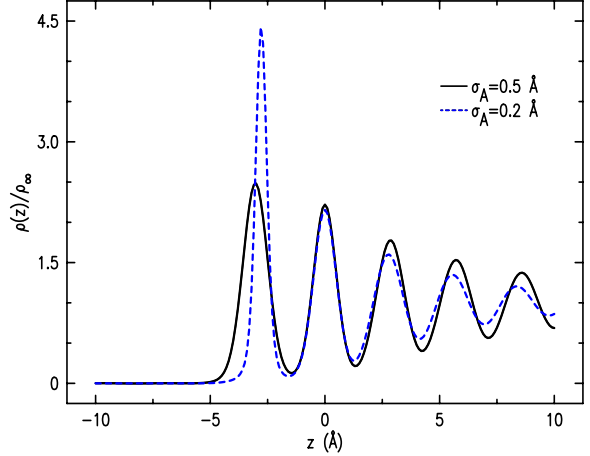


FIG. 6. (Color online) The electron densities  $\langle \rho(z) \rangle / \rho_\infty$  corresponding to the two fits of the present model to the measured Bi reflectivity are shown in Fig. 4.

larger than the distance between planes of close-packed spheres with this atomic diameter ( $3.1\sqrt{2/3}\text{\AA}=2.53 \text{ \AA}$ ). In fact, although with increasing  $\eta$  the specular reflectivity signal rapidly decreases in comparison with the diffuse scattering signal from the bulk liquid, the analysis presented in Appendix B assures that the background-subtracted  $R/R_F$  curves reported here are reliable.

The dotted line in Fig. 4 indicates that—similar to the case for Sn—the best fit of the simple DCM to the measured Bi reflectivity underestimates the low- $q_z$  reflectivity. Although the effect is not as strong as for Sn, it is clearly outside of the statistical error bars. As discussed above for Sn and illustrated in Appendix A, the discrepancy between the data and the DCM is an unambiguous indication that the electron density near the surface is larger than in the bulk. The best fits for  $\sigma_A=0.2 \text{ \AA}$  and for  $0.5 \text{ \AA}$  overlap so well that they can only be distinguished in the figure at large  $q_z$ . The electron densities for these two fits are drawn in Fig. 6. The figure illustrates that—as for Sn—the best-fit model appears to be sensitive only to the integrated density of the adlayer and the detailed shape of the adlayer cannot be extracted from the reflectivity. The graphs illustrate that—as for Sn—the amplitude of the Bi rich surface adlayer is not a unique measure of the source of the low- $q_z$  maximum in  $R(q_z)$ .

These points are further emphasized by the results shown in Fig. 7(a). The values of  $\rho_A$  are all larger than unity. On the other hand, and as shown in Fig. 7(b), in contrast to the case of Sn the first layer for Bi is systematically diluted.

A more direct comparison between the surface layering of Sn and Bi is demonstrated in the plots of the interfacial structure factor (squared),

$$\frac{R(q_z)}{R_F(q_z) \int_{A_{xy}^{q_{xy}}} d^2 q_{xy} (q_{xy}/q_{\max})^\eta (\eta/2\pi q_{xy}^2)} \approx |\Phi(q_z)|^2, \quad (12)$$

in Fig. 8, where the effects of the common  $R_F$  and different thermal capillary waves' smearing factors have been re-

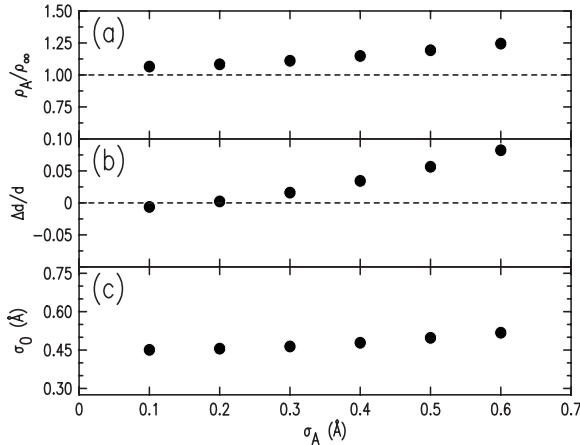


FIG. 7. Parameters derived from the best-fit models for the Bi data as a function of the different fixed values of  $\sigma_A$ .

moved. For  $q_z \leq 2.0 \text{ \AA}^{-1}$ , the two surface structure factors are nearly identical. Unfortunately, the size of the error bars for the Bi data at  $q_z > 2.0 \text{ \AA}^{-1}$  makes it difficult to know precisely how much larger  $|\Phi(q_z)|$  is for Bi than for Sn in this  $q_z$  range, but it is clear that although  $R/R_F$  for Bi is lower than that of Sn, the structure factor for Bi is certainly not smaller than that of Sn. The inset displays the same data normalized to  $q_{\text{peak}}$  the layering peak position. On this scale, the coincidence of the two curves is even closer.

Another way to see this effect is to compare  $\langle \rho(z) \rangle / \rho_\infty$  for Sn and Bi calculated under the assumption that the width of the surface adlayer is essentially equal to the width of the first layer in the DCM. This is shown in Fig. 9 for the example of  $\sigma_A=0.5 \text{ \AA}$ . The curves seem to indicate that although the ratio of the electron density of the first two surface layers to the bulk density is essentially the same for Sn and Bi, the length scale over which the surface layering decays is significantly shorter for Sn than for Bi. This effect can be seen in Fig. 10 where the values of the Gaussian decay parameter  $\Lambda=1/\bar{\sigma}$  for Sn and Bi are plotted for a

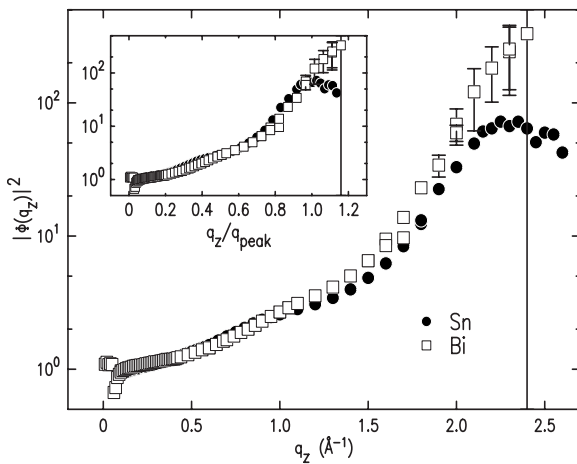


FIG. 8. Comparison of the measured liquid surface structure factors for Sn (●) and Bi (□). Inset: the same data plotted vs  $q_z/q_{\text{peak}}$  where  $q_{\text{peak}}=2.07 \text{ \AA}^{-1}$  for Bi and  $2.29 \text{ \AA}^{-1}$  for Sn. There are only slight differences between the two curves.

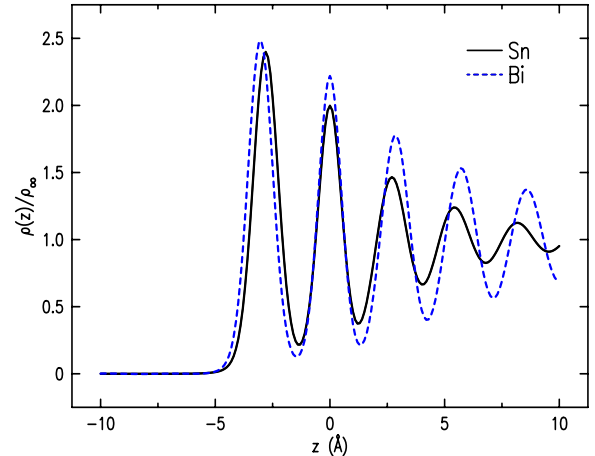


FIG. 9. (Color online) Comparison between the surface electron-density models for Sn and Bi fitted assuming an equal width of  $\sim 0.5 \text{ \AA}$  for the top adlayer and the adjacent first DCM layer.

range of  $\sigma_A$ . As can be seen, the values of  $\Lambda$ , like other parameters that were shown above, are relatively insensitive ( $\sim 20\%$ ) to the assumed values of  $\sigma_A$ . We also note that  $\Lambda$  of Bi is systematically larger (by  $\sim 40\%$ ) than  $\Lambda$  of Sn.

## V. SUMMARY

Prior to the measurements of the surface order of liquid Sn and Bi, all of the metals that had been studied (Ga, In, and K) except Hg had essentially identical surface structure factors that could be satisfactorily explained by a simple distorted crystal model. As predicted by Rice,<sup>1,2</sup> the necessary change in the electronic structure between a sea of delocalized conduction electrons in equilibrium with a liquid of charged ionized atoms and a vapor of neutral atoms gives rise to atomic layering that decays monotonically with distance from the surface. The present observation of an enhanced near-surface electron density in Bi is very similar to

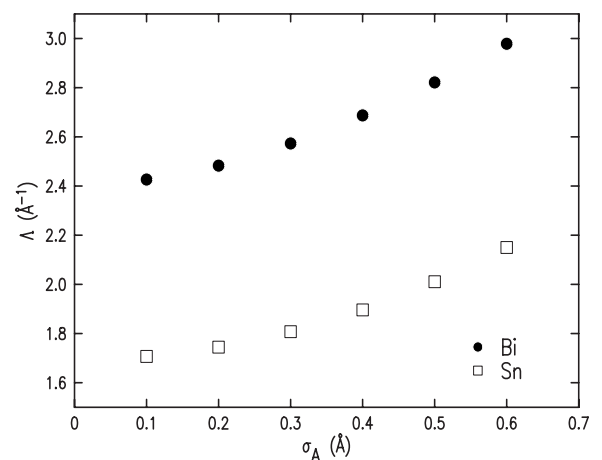


FIG. 10. Gaussian decay parameter,  $\Lambda=1/\bar{\sigma}$ , for Sn and Bi. The differences are larger than could be accounted for by the atomic sizes alone.

that found in Sn (Ref. 8) and is different from that of other liquid metals studied to date. Although Ref. 8 reported that the Sn surface could be explained by a model in which the spacing between the first and second layers was compressed by  $\sim 10\%$ , the present analysis indicates that that result was for only one specific model. The data for both Bi and Sn can be explained by different models; the common feature of which is a topmost monolayer having an integrated density that is higher than the bulk density. Furthermore, when the surface-roughening effects of the thermal capillary waves are removed, the bare surface structure factors of Sn and Bi are remarkably similar. The principal difference between the two is that the layering in Bi penetrates significantly deeper below the surface than in Sn. In fact the Gaussian decay parameter  $\Lambda$  is  $\sim 40\%$  larger for Bi than for Sn. This difference cannot be explained by the difference in the atomic sizes which is of the order of 10%.<sup>13</sup>

No theoretical explanation can be offered at this time for the difference in the surface-normal structure between Bi and Sn on one hand and Ga, In, and K on the other hand. Furthermore, the case of Hg remains an isolated example that is different from all of the other metals that have been studied. There is a clear need for theoretical work on this problem.

## ACKNOWLEDGMENTS

This work has been supported by the U.S. Department of Energy through Grant No. DE-FG02-88-ER45379 and ChemMatCARS is principally supported by the National Science Foundation/Department of Energy under Grant No. CHE0087817. The Advanced Photon Source is supported by the U.S. Department of Energy, Basic Energy Sciences, Office of Science under Contract No. W-31-109-Eng-38.

## APPENDIX A: STRUCTURE FACTOR OF THE MODIFIED DCM MODEL

This model modifies the DCM model by adding a topmost single layer of variable density and width represented by a single Gaussian as given in Eq. (11) in the main text. The effect of the amplitude of the adlayer on the shape of the  $q_z$  dependence of the surface structure of this model can be visualized by taking the Fourier transform of the convolution of the atomic form factor with the atomic density distribution in Eq. (11). This yields the structure factor of the interface,

$$\Phi(q_z) = \Phi^A(q_z) + \Phi^{\text{DCM}}(q_z), \quad (13)$$

where  $\Phi^{\text{DCM}}(q_z)$  is given by Eq. (10) and

$$\Phi^A(q_z) \approx (q_z d)[F(q_z)/Z_{\text{eff}}]\rho_A \exp[-iq_z d_A] \exp[-q_z^2 \sigma_A^2/2]. \quad (14)$$

$|\Phi^A(q_z)|^2$  and  $|\Phi^{\text{DCM}}(q_z)|^2$  are plotted in Fig. 11 for the best-fit Bi parameters corresponding to  $\sigma_A=0.2$  Å. However, the results are essentially unchanged for  $\sigma_A=0.5$  Å. A polar plot of the complex function  $\text{Re}[\Phi(q_z)]+i\text{Im}[\Phi(q_z)]$  is shown in the insert for  $3\pi/2d > q_z > 0$ . With increasing  $q_z$ , the phase difference between  $\Phi^A(q_z)$  and  $\Phi^{\text{DCM}}(q_z)$  increases from zero; but since  $|\Phi^A(q_z)|^2 > |\Phi^{\text{DCM}}(q_z)|^2$  for most of the relevant

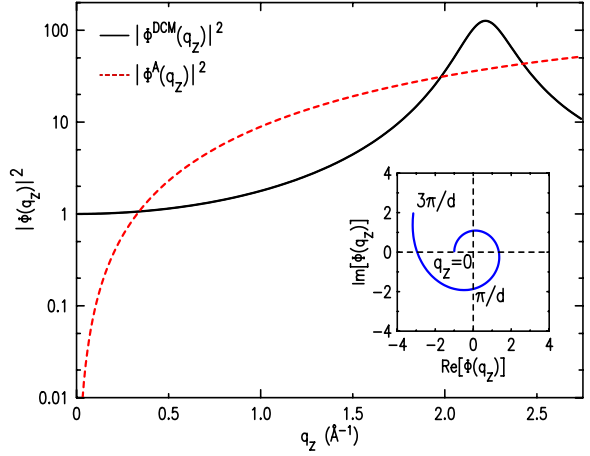


FIG. 11. (Color online) Plot of the squares,  $|\Phi^A(q_z)|^2$  (---) and  $|\Phi^{\text{DCM}}(q_z)|^2$  (—), of the two additive terms of the surface structure factor  $\Phi(q_z)$  [see Eq. (13)] for the best-fit parameters of Bi for  $\sigma_A=0.2$  Å. Inset: polar plot of  $\text{Re}[\Phi(q_z)]+i\text{Im}[\Phi(q_z)]$  in the range  $3\pi/2d > q_z > 0$ .

range approaching  $q_z d \sim \pi$ , the amplitude  $|\Phi(q_z)|^2 > |\Phi^{\text{DCM}}(q_z)|^2$ . The effect of increasing  $\rho_A$  is demonstrated by the curves in Fig. 12. For  $\rho_A < 1$  (i.e.,  $\rho_A=0.8$ ), the amplitudes of  $\Phi^A(q_z)$  and  $\Phi^{\text{DCM}}(q_z)$  are close enough to each other to cause destructive interference which produces a pronounced minimum when  $q_z \approx \pi/d=1.1$  Å<sup>-1</sup>. With increasing  $\rho_A$ , the depth of the minima decreases. The fact that the  $|\Phi(q_z)|^2 > 1$  behavior at small  $q_z$  is not followed by a visible minimum in which  $|\Phi(q_z)|^2 < 1$  is an unambiguous demonstration that the amplitude of the adlayer is larger than unity.

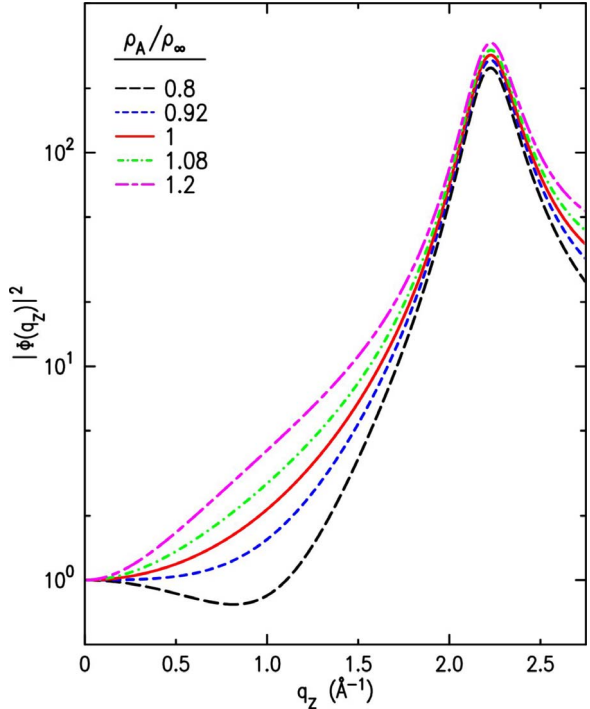


FIG. 12. (Color online) The surface structure factor squared for  $\rho_A/\rho_\infty=0.8, 0.92, 1.0, 1.08$ , and  $1.2$ . The values for the other parameter are those of the best fits for Bi at  $\sigma_A=0.2$  Å.

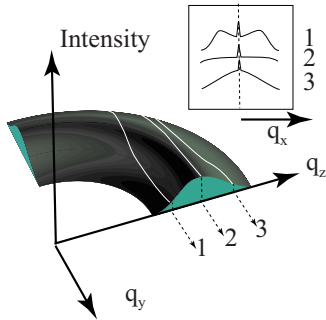


FIG. 13. (Color online) Schematic illustrating the shape of the bulk diffuse scattering underlying the specular peak in the  $q_{xy}$ - $q_z$  plane. The inset illustrates the shape of the measured intensity as a function of  $q_x$  at  $q_z$  smaller than the peak in the bulk diffuse scattering (1), at the peak (2), and larger than the peak (3).

#### APPENDIX B: DISTINGUISHING THE SPECULAR SIGNAL FROM THE BULK DIFFUSE SCATTERING

At  $q_z$  values close to that of the liquid bulk peak, the diffuse bulk scattering may be much larger than the specular signal. Nevertheless, in view of the fact that the specular signal only appears in the plane of incidence ( $\theta=0$ ) and at an angle  $\beta=\alpha$ , it can be easily separated out of the measured signal. The schematic in Fig. 13 illustrates the intensity distribution of the diffuse scattering from the bulk liquid. The maximum along the circular region in the  $q_z$ - $q_{xy}$  plane corresponds to the intensity near the peak of the bulk diffuse scattering. The sharp specular reflection ridge (not shown on the main figure) extends along the  $q_z$  axis. The inset illustrates the shape of the intensity that is measured as  $\theta$  is scanned across the specular condition at  $q_{xy}=0$  for  $q_z < q_{\text{peak}}^{\text{bulk}}$  (trace 1), for  $q_z = q_{\text{peak}}^{\text{bulk}}$  (trace 2), and for  $q_z > q_{\text{peak}}^{\text{bulk}}$  (trace 3). For trace 1, the value of  $q_z < q_{\text{peak}}^{\text{bulk}}$ , however, as  $|q_x| \approx (2\pi/\lambda)\cos\alpha|\sin\theta|$  increases  $\sqrt{q_x^2 + q_z^2} \rightarrow q_{\text{peak}}^{\text{bulk}}$  and the diffuse scattering intensity increases. Trace 1 in the inset illustrates that the specular peak at  $q_x=0$  is superposed on the diffuse background that has a minimum at  $q_x=0$ . The bulk diffuse scattering in the sketch for trace 3, which corresponds to  $q_z > q_{\text{peak}}^{\text{bulk}}$ , is peaked at  $q_x=0$  and decreases as  $\sqrt{q_x^2 + q_z^2}$

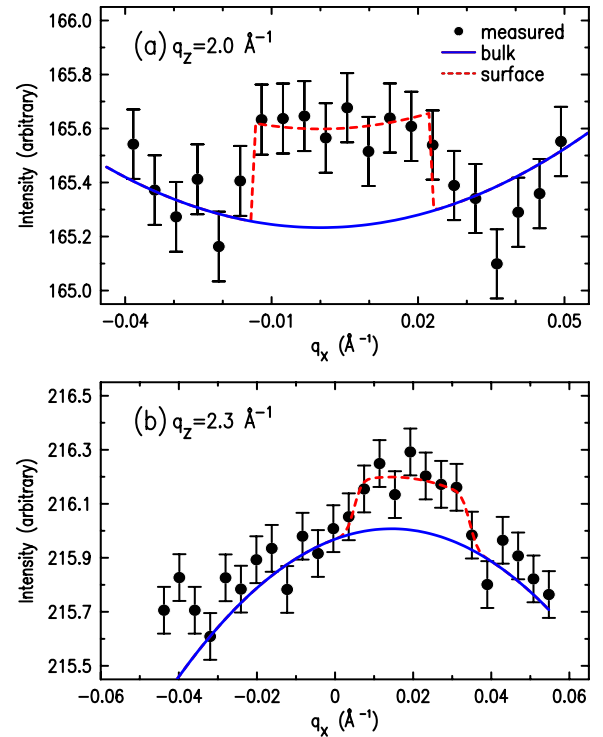


FIG. 14. (Color online) Measured intensity as a function of  $q_x$  for  $q_z=2.0 \text{ \AA}^{-1}$  and  $2.3 \text{ \AA}^{-1}$  (●). The solid and dashed lines indicate, respectively, the theoretically expected shape of the diffuse scattering from the bulk liquid and the specularly reflected beam from the surface.

$-q_{\text{peak}}^{\text{bulk}}$  increases. Examples of these scans are shown in Fig. 14 for  $q_z=2.0 \text{ \AA}^{-1}$  and  $2.3 \text{ \AA}^{-1}$ . The solid lines indicate the shape predicted for the intensity of the bulk diffuse scattering on the basis of the bulk liquid structure factor measured in our experiment, while the dashed lines are the intensities of surface reflections. Our measured data agree with that reported in the literature.<sup>14</sup> It is clear that  $q_z \approx 2.3 \text{ \AA}^{-1}$  is close to the limiting value at which the specular signal for Bi can be measured with the current resolution.

- <sup>1</sup>S. A. Rice, Proc. Natl. Acad. Sci. U.S.A. **84**, 4709 (1987).
- <sup>2</sup>M. P. D'Evelyn and S. A. Rice, Phys. Rev. Lett. **47**, 1844 (1981).
- <sup>3</sup>M. P. Allen and D. J. Tildesley, *Computer Simulation of Liquids* (Clarendon, New York/Oxford University Press, Oxford, 1987).
- <sup>4</sup>M. J. Regan, E. H. Kawamoto, S. Lee, P. S. Pershan, N. Maskil, M. Deutsch, O. M. Magnussen, B. M. Ocko, and L. E. Berman, Phys. Rev. Lett. **75**, 2498 (1995).
- <sup>5</sup>H. Tostmann, E. DiMasi, P. S. Pershan, B. M. Ocko, O. G. Shpyrko, and M. Deutsch, Phys. Rev. B **59**, 783 (1999).
- <sup>6</sup>O. G. Shpyrko, P. Huber, A. Y. Grigoriev, P. S. Pershan, B. Ocko, H. Tostmann, and M. Deutsch, Phys. Rev. B **67**, 115405 (2003).
- <sup>7</sup>O. M. Magnussen, B. M. Ocko, M. J. Regan, K. Penanen, P. S.

- Pershan, and M. Deutsch, Phys. Rev. Lett. **74**, 4444 (1995).
- <sup>8</sup>O. G. Shpyrko, A. Y. Grigoriev, C. Steimer, P. S. Pershan, B. Lin, M. Meron, T. Graber, J. Gerhardt, B. Ocko, and M. Deutsch, Phys. Rev. B **70**, 224206 (2004).
- <sup>9</sup>V. S. K. Balagurusamy, R. Streitel, O. G. Shpyrko, P. S. Pershan, M. Meron, and B. Lin, Phys. Rev. B **75**, 104209 (2007).
- <sup>10</sup>O. G. Shpyrko, A. Y. Grigoriev, R. Streitel, D. Pontoni, P. S. Pershan, M. Deutsch, B. Ocko, M. Meron, and B. H. Lin, Phys. Rev. Lett. **95**, 106103 (2005).
- <sup>11</sup>P. S. Pershan, Colloids Surf., A **171**, 149 (2000).
- <sup>12</sup>P. S. Pershan, J. Phys. Chem. B (to be published).
- <sup>13</sup>J. Emsley, *The Elements* (Clarendon, Oxford, 1998).
- <sup>14</sup>S. Takeda, S. Tamaki, and Y. Waseda, J. Phys. Soc. Jpn. **54**, 2552 (1985).